



Article

Edge Detection of Source Body from Magnetic Anomaly Based on ResNet

Xinyi Zhou ¹, Zhaoxi Chen ^{1,2,*}, Hong Chen ¹, Shuai Wang ¹ and Zenzele Osborne Kubeka ¹

¹ School of Geophysics and Information Technology, China University of Geosciences (Beijing), Beijing 100083, China; 2010200034@email.cugb.edu.cn (X.Z.); 2010190035@email.cugb.edu.cn (H.C.); wangs@email.cugb.edu.cn (S.W.); 9110190001@email.cugb.edu.cn (Z.O.K.)

² Key Laboratory of Intraplate Volcanoes and Earthquakes (China University of Geosciences, Beijing), Ministry of Education, Beijing 100083, China

* Correspondence: zxchen@cugb.edu.cn

Abstract: Utilizing magnetic anomaly data for effective edge detection of source bodies can provide crucial evidence for the delineation of geological units and the division of fault structures. However, the existing edge detection methods of source bodies from magnetic anomalies are influenced by factors such as the source bodies' burial depth, magnetization direction, and mutual interference of magnetic anomalies, leading to errors in subsequent interpretation tasks. The advanced convolutional neural network possesses robust capabilities for feature representation and deep learning, prompting this paper to introduce an edge detection method for source bodies based on convolutional neural networks. The issue is initially framed as a semantic segmentation problem, and four network architectures aimed at edge detection of a source body from magnetic anomaly are designed and modified based on the U-Net and ResNet. Subsequently, a multitude of high-quality sample data sets are constructed using models with varying locations, scales, quantities, and physical properties to train the network. This paper then details model experiments that escalate from simple to complex, taking into account the combined effects of burial depth and inclined magnetization on edge detection. Compared to conventional edge detection methods, the method proposed in this paper is shown to accurately identify edges of source bodies at various depths with little impact from inclined magnetization and can automatically extract edge information without manual intervention. The method's efficacy is corroborated through real data tests.



Citation: Zhou, X.; Chen, Z.; Chen, H.; Wang, S.; Kubeka, Z.O. Edge Detection of Source Body from Magnetic Anomaly Based on ResNet. *Remote Sens.* **2024**, *16*, 4139. <https://doi.org/10.3390/rs16224139>

Academic Editor: Stefano Perna

Received: 23 September 2024

Revised: 25 October 2024

Accepted: 4 November 2024

Published: 6 November 2024



Copyright: © 2024 by the authors. Licensee MDPI, Basel, Switzerland. This article is an open access article distributed under the terms and conditions of the Creative Commons Attribution (CC BY) license (<https://creativecommons.org/licenses/by/4.0/>).

Keywords: magnetic anomaly; edge detection; deep learning; convolutional neural networks; residual networks

1. Introduction

Edge detection of a source body from magnetic anomaly is a method for the identification of the boundary positions of magnetic targets. It fully leverages the high lateral resolution advantage of magnetic anomaly data, and is the core of magnetic anomaly data processing and interpretation. Existing edge detection methods can be broadly classified into three main categories based on technical principles: numerical calculation, mathematical statistics, and others [1].

Edge detection based on numerical calculation involves processing anomaly data or its gradient data through numerical computations, revealing boundary information as extreme or zero values. This approach is also one of the most extensively studied and widely applied methods to date [2–9]. These methods identify boundary positions by calculating the modulus from potential field or gradient tensor data, and their common shortcoming is inaccurate edge detection for targets at greater depths. To address this issue, many methods [10–12] have been developed to more evenly detect the boundaries of target bodies at various depths, capable of identifying targets with significant amplitude differences, but their resolution tends to be lower. To enhance the resolution of

detection results, higher-order derivatives have been incorporated into edge detection methods [13–16]. Although edge detection methods based on higher-order derivatives can effectively improve the resolution of detection results, the noise is also amplified after higher-order derivative operations, which can affect the effectiveness of edge detection. Statistical-based edge detection methods utilize sliding windows and probability statistics to extract the edge information of target bodies [17–19]. These statistical edge detection methods, while capable of suppressing noise interference, tend to identify edges with broader features and lower resolution. Other edge detection methods are primarily used in some specific issues of edge detection like imaging or enhancement [20–22]. In recent years, novel edge detection methods have been proposed [23–27]. However, with the number of edge detection methods and their applications becoming overwhelming, errors and misinterpretations of edge detection filters have multiplied [28]. Liu et al. [29] proposed another classification of potential field edge detectors/filters, including derivative-based, phase- or ratio-based and statistical/sliding window-based methods.

With the development of artificial intelligence, convolutional neural networks (CNNs), with their strong feature extraction and nonlinear fitting capabilities, have been widely applied in the field of geophysical denoising [30–34] and geophysical inversion [35–41]. Currently, there are relatively few studies in the field of edge detection of a source body from magnetic anomaly based on deep learning [42]. However, deep learning is extensively applied in the field of remote sensing object recognition [43,44]. Li et al. [45] used the AlexNet network to detect buildings in high-resolution images of hollow villages. Pan et al. [46] improved the fully convolutional neural network for extracting residential areas from “Gaofen-1” remote sensing imagery. Wang et al. [47] enhanced the feature extraction capability of lightweight networks through a dual-path semantic segmentation structure. Lan et al. [48] proposed the GD-DCNN for road segmentation and confirmed that the network reduces the effects of noise and occlusions.

Remote sensing object recognition based on deep learning involves using deep neural networks to learn the mapping relationship between target bodies and their corresponding spectral features, thereby achieving intelligent recognition of remote sensing objects. Similarly, the deep learning-based edge detection of a source body from magnetic anomaly proposed in this paper is about using deep neural networks to learn the mapping relationship between the boundaries of magnetic target bodies and their corresponding magnetic anomaly features. This introduces a new perspective to the field of edge detection of a source body from magnetic anomaly. Exploring the application of deep learning in this area can harness unique advantages over traditional edge detection methods.

2. Edge Detection Method by Deep Learning

Edge detection is an important technique in potential field data processing. Conventional edge detection methods (e.g., vertical derivative method [6], total horizontal derivative method [7], analytic signal method [9], tilt angle method [10] and theta map method [12], etc.) tend to produce blurred or distorted results when dealing with deep anomaly targets. Although improved methods using higher-order derivatives can identify the edges of deep anomalies more effectively, they are computationally complex and prone to noise interference. In contrast, deep learning methods employ deep neural networks to extract and learn the end-to-end mapping relationships between magnetic anomaly features and the edges of magnetic susceptibility model’s horizontal projection. This process does not require human intervention, significantly reducing the influence of subjective factors.

2.1. The Feasibility of Edge Detection by Deep Learning

The deep learning edge detection method for magnetic anomalies presented in this paper is achieved by the neural network directly learning the end-to-end mapping function from the magnetic anomaly data to the horizontal projection edge of the magnetization model, and its function is as follows:

$$p = F(\Delta T), \quad (1)$$

where p represents the horizontal projection edge of the model; ΔT represents the magnetic anomaly data; F is the mapping function.

Typically, regardless of how the magnetization angle of the model changes, the frame of its projection boundary only exists near the magnetic anomaly extremes or inflection points. Its horizontal position corresponds well to the ground reality, and there is no need to enclose an infinitely large range of magnetic anomalies for the projection boundary (as would be the case in one-dimensional space). These two have a certain spatial correlation and local existence [42], and the convolution operations commonly used in deep learning can precisely learn the locality and spatiality of the input image and the output label [49]. This provides feasibility for deep learning to identify the edges of magnetic anomaly source bodies.

In the field of deep learning-based remote sensing image object recognition, one of the most common methods is image semantic segmentation, which classifies each pixel in the image based on the spectral and spatial structural features of the remote sensing images [45,46]. In the study of deep learning-based edge detection for magnetic anomalies, the input is the observed magnetic anomaly data, which is similar to two-dimensional continuously varying image data, and the output is the horizontal projection edge m of the magnetization model, resembling two-dimensional binary label data composed of 0 s and 1 s, akin to a pixel classification problem. Essentially, edge detection can also be viewed as a kind of image semantic segmentation problem, requiring each pixel in the magnetic anomaly image to be classified, with those belonging to the horizontal projection boundary of the source body as one category; and the non-boundary ones as another category. Thus, the edge detection problem transforms into an image semantic segmentation problem, for which the network structure can adopt commonly used semantic segmentation network models.

2.2. Network Structure Design

At present, the mainstream semantic segmentation model is the encoder–decoder structure. The U-Net network proposed by Ronneberger et al. [50] in 2015 is a completely symmetric encoder–decoder structure, which has been proven to achieve better prediction results with fewer training samples. This is very important for geophysical fields with less training data and has become one of the most commonly used deep learning networks in the field of geophysics. This paper selects the original U-Net as the basic network. In order to apply it to edge detection problems, this paper simplifies and modifies it to obtain a network suitable for edge detection problems. Four types of edge detection networks (EDNs) are obtained by secondary modification of the network using convolutional block stacking and residual connection blocks. These four types of networks are as follows: (1) U-Net EDN, mainly modified to reduce the number of channels to adapt to magnetic anomaly data; (2) convolution block stacking EDN, which increases the depth of the network by stacking convolutional blocks to improve performance; (3) the ResNet-34 EDN and (4) the ResNet-50 EDN introduce conventional residual blocks and bottleneck residual blocks [51], respectively, to solve the problem of network degradation caused by the excessive depth of the network.

To design a CNN base on U-net, we usually consider the convolution, activation function, BN (batch normalization) [52], down-sampling, up-sampling, etc. Convolution is a special linear operation for extracting local features of input data. The convolution kernel slides over the input data, computing the dot product with the overlapping region at each step and then summing these values. Different kernel size, stride and padding will produce different results. The activation function is the addition of nonlinear factors to neural networks. It is also sometimes able to normalize the data, and map the input data to a certain range. The BN layer normalizes the input of each batch of data, and induces scaling and shifting parameters for the network to learn the optimal feature distribution.

The BN makes the distribution of input data in each layer of the network relatively stable, accelerating model training and convergence speed. Down-sampling and up-sampling refer to the spatial size variation operations of feature maps. Down-sampling, also known as pooling, often selects the maximum or mean value as the sampling point in each region of the feature map, in order to reduce the spatial size of the feature map. Up-sampling includes deconvolution/transpose convolution and interpolation, where deconvolution operation up-samples by learning a reversible convolution kernel, while the interpolation operation fills and interpolates the feature map through interpolation algorithms such as nearest neighbor interpolation, bilinear interpolation, etc., thereby increasing the size of the feature map.

2.3. U-Net Edge Detection Network

Based on the network architecture of U-net, this paper designs and builds a U-net EDN to realize the deep learning edge detection of a magnetic anomaly. The magnetic anomaly data obtained by forward calculation are used as the training data of the input layer. Since there is only one layer of magnetic anomaly data on the ground, the number of RGB channels of the original input layer is reduced to one channel. The output layer is the boundary of the horizontal projection of the magnetic field source body. Whether it is the boundary is indicated by 1 and 0. It is a single classification problem, so the number of channels is also 1.

There are a total of 15 layers in the network that use convolutional operations, as excessive convolutional kernel dimensions can lead to an increase in training parameters, resulting in a slower operation speed. However, if the convolutional kernel is too small, it will cause the receptive field to be too small. Therefore, the dimension of the convolutional kernel in this article is 3×3 . The 3-layer down-sampling layer adopts maximum pooling operation, while the 3-layer up-sampling layer adopts transposed convolution operation. Except for the output layer, the activation functions of all other layers use the ReLU (Rectified Linear Unit) function [53]. Compared with other activation functions, the ReLU function is computationally simple, requiring only positive and negative inputs to obtain the activation value, which improves the speed of operation. Moreover, the ReLU function, in the area where the input is greater than zero, will not have the problems of gradient explosion and gradient disappearance. The sigmoid function is used as the output layer activation function [54].

The U-net EDN is mainly composed of encoding and decoding stages. The encoding stage is a contraction path to extract the characteristics of the input data. With the increase in the number of down-sampling layers, the data dimension is gradually reduced. After each down-sampling, the data dimension is reduced by half, but the corresponding number of convolution kernels becomes twice as large. In the U-net EDN, the shallow network layer extracts local information, and the deeper network layer extracts global information. Its overall architecture is shown in Figure 1.

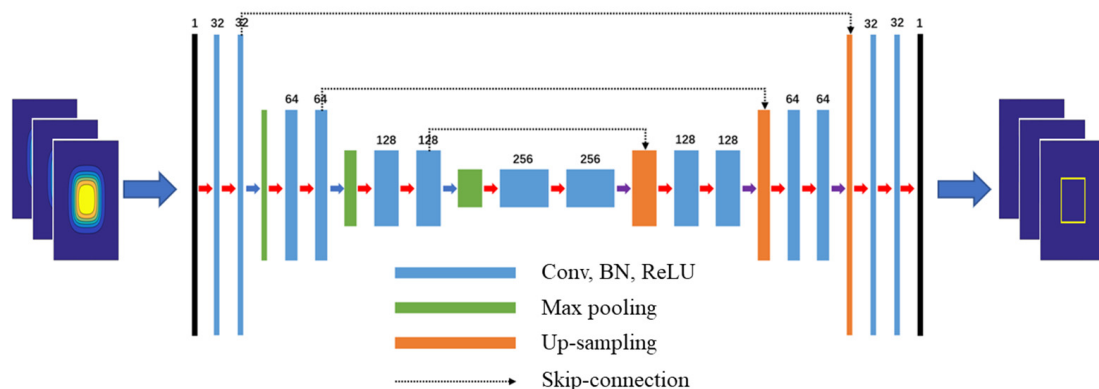


Figure 1. U-Net edge detection network.

As shown in Figure 1, the black number above the feature map represents the number of channels, and the light blue layer represents the convolution layer of convolution, BN and ReLU operation. The green layer represents the down-sampling layer using the maximum pooling operation, and the black dotted line represents the “skip-connection”. In the coding stage, in order to extract the global features, the receptive field is often increased by down-sampling, but the high-level feature dimension is reduced. In order to achieve end-to-end mapping, it is necessary to restore the high-level feature dimension to the size of the input data dimension. This process is called up-sampling in the neural network, and the brown layer represents the up-sampling layer using transpose convolution operation. While down-sampling lost lots of information in coding stage, skip connection can introduce feature information at corresponding scales into the up-sampling process.

2.4. Convolution Block Stacking Edge Detection Network

The simplest and most effective way to further improve the network’s ability to learn complex mappings is to stack convolutional layers to increase the depth of the network. This article modifies the encoding stage structure of the EDN by expanding the convolutional layer from the original convolution–convolution–pooling structure, as shown in Figure 2. Comparing Figure 1 with Figure 2, it can be observed that the EDN with stacked convolutional blocks has expanded some convolutional modules. In the feature extraction stage before the first down-sampling, the convolutional layers have expanded by one layer and three convolutional modules. The number of convolutional layers in the feature extraction stage before the second down-sampling is expanded into one layer convolution and four layer convolution modules. The number of convolutional layers in the feature extraction stage before the third down-sampling is expanded into one layer convolution and six layer convolution modules. The convolutional layers in the feature extraction stage before up-sampling are expanded into one layer convolution and three layer convolution modules.

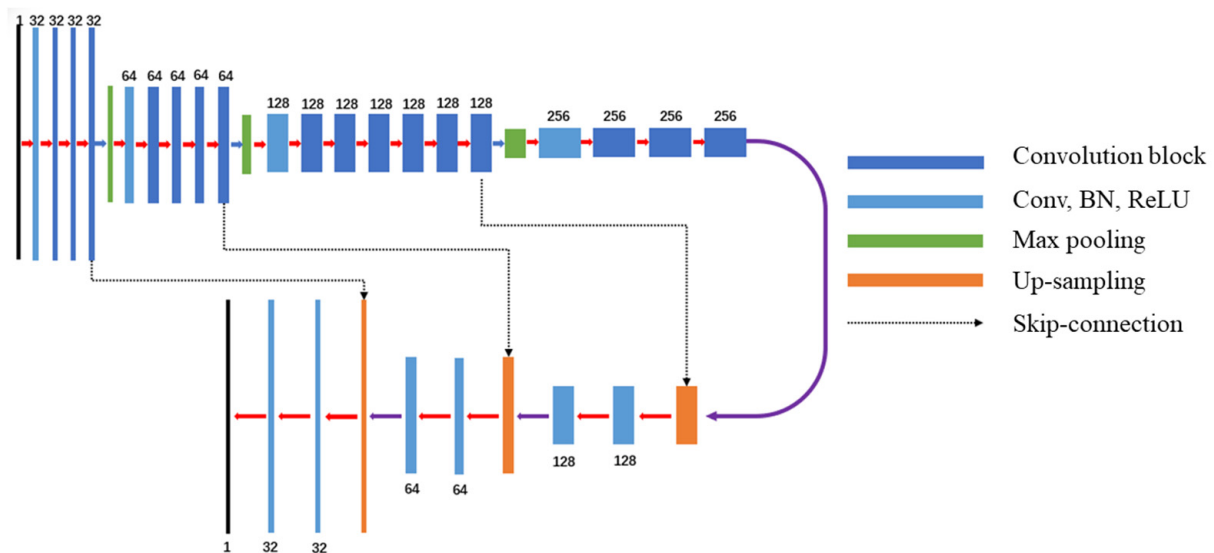


Figure 2. Convolution block stacking edge detection network.

2.5. ResNet Edge Detection Network

The stacking of convolution blocks is the most direct way to improve network performance, but an excessive increase in network depth can degrade network performance. The best way to solve this problem is to convert convolution block stacking into residual block stacking. Due to the residual characteristics between any residual blocks, residual block stacking will not cause gradient instability and the network will not experience degradation. At present, residual blocks can be divided into two categories based on ResNet-50: the one before ResNet-50 is the conventional residual block; the bottleneck residual block

after ResNet-50 is shown in Figure 3. Figure 3a shows the conventional residual block, with each residual block consisting of two convolutional layers. The output of the second convolutional layer and the input of the residual block are added and activated using the ReLU function to obtain the output of the residual block, with a parameter size of 18,432. As shown in Figure 3b, the bottleneck residual block deepens the network depth without significant differences in parameter quantities.

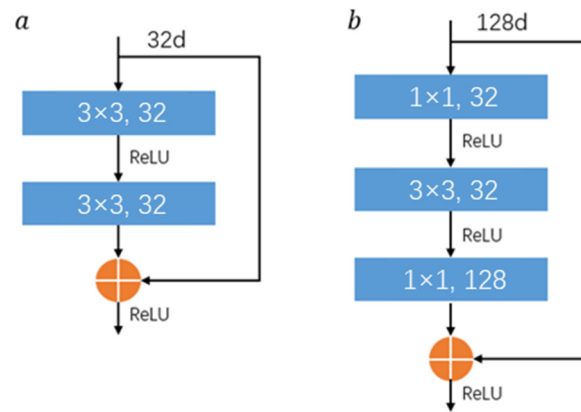


Figure 3. Residual block [51]. (a) Conventional residual block. (b) Bottleneck residual block. The numbers in the blue box present filter size (e.g., 3×3) and channel (e.g., 32). And d presents the dimension of the input.

The convolution blocks of the convolution block stack EDN described above are all replaced by the conventional residual module, that is, the improved EDN based on ResNet-34 is obtained. The conventional residual module of ResNet-34 EDN is replaced by the bottleneck residual block, and the number of characteristic diagrams of each layer is increased by four times, that is, the improved EDN based on ResNet-50 is obtained. The structure and parameters of ResNet-50 EDN are the same, except that the structure of characteristic graph channel and residual block is different from ResNet-34 EDN.

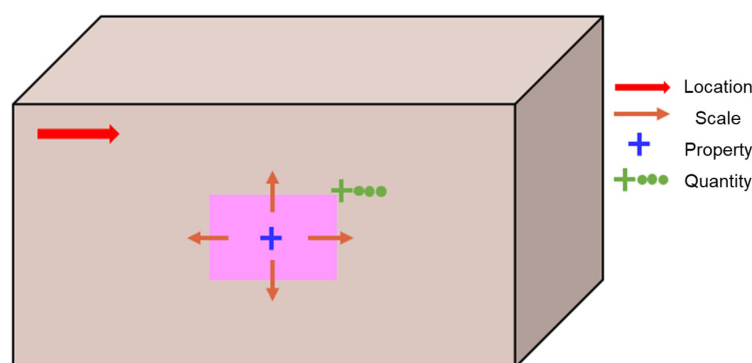
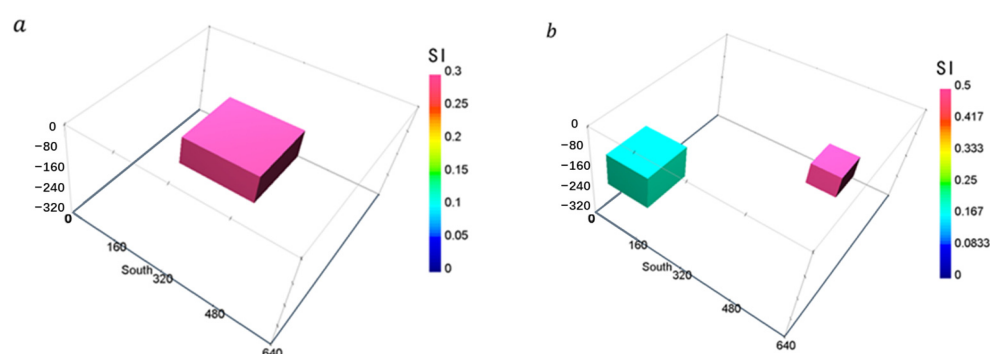
3. Dataset and Network Training

3.1. Establishment of Magnetic Anomaly Dataset

In this task, the design of the observation system includes two parts: the design of the surface survey grid and the design of the subsurface half space mesh. The details of the design standard are shown in Table 1. In this paper, the input data are obtained by magnetic anomaly forward modeling. The boundary of the magnetic anomaly source body projected on the horizontal plane is taken as the label data. The input data and label data form a training data pair, and then a large number of training data pairs form a training data set. The acquisition process of input data is divided into two steps: the construction of the subsurface model and forward modeling of the magnetic anomaly. In this paper, the subsurface model is constructed by using parameters such as quantity, location, scale and physical properties, and some of these parameters are shown in Table 1. Firstly, the coordinate of the model center point is determined in the variation range. And then the model extension length (the length, width and height of model) is randomly generated within the range. The subsurface model is formed by the combination of various parameters, including a single block model and combined block model. The random variation process of the model is shown in Figure 4. In addition, considering the actual rock magnetic susceptibility, the variation range of residual magnetic susceptibility of each block is set as $-0.3 \sim 0.8$ SI. In order to prevent the influence of edge data on the experimental error, we discard the model close to the 20 m edge of the mesh in the subsurface half space. The perspective view of the single block and combined block model is shown in Figure 5.

Table 1. Establishment standard of mesh, grid and model.

Parameter	Value		
	X	Y	Z
Mesh number of subsurface	64	64	32
Mesh size of subsurface (m)	10	10	10
Grid number of observation	64	64	/
Coordinate of model center point (m)	40–600	40–600	30–125
Model extension length (m)	40–450	40–450	80–200

**Figure 4.** The random variation process of the model in the subsurface half space.**Figure 5.** The perspective view of model. (a) Single block model. (b) Combined block model.

The dataset of the network consists of two parts, one is input data and the other is label data. In this paper, the input data are the magnetic anomaly of the magnetic target with the forward process [55]. And 20,000 models are randomly generated according to the distribution range of various model parameters proposed in the model design, including a single block model and a combined block model. The geomagnetic field and magnetization direction remain consistent, with a magnetic inclination of 3° within the range of $(0-90^\circ)$, divided into 30 categories. The magnetic declination is also divided into 30 categories within the range of $(0-90^\circ)$, and a random combination of magnetic inclination and magnetic declination generates a total of 900 different combinations. We randomly select types from the combination of magnetic inclination and magnetic declination angle, and performs forward calculation on the block model designed in the previous section based on a total magnetic field strength of 50,000 nT to obtain forward magnetic anomalies. The quality of label data affects the training results of the network, so labels must be designed strictly according to the requirements of the task. The research task of this article is to use deep learning networks for edge detection of magnetic target bodies, so the label data are designed as the boundaries of the magnetic field source body projected on a horizontal plane. Figure 6a shows the input data, namely magnetic anomalies. Figure 6b shows the labeled data, where the yellow pixel shows the horizontal projection boundary of the magnetic field source.

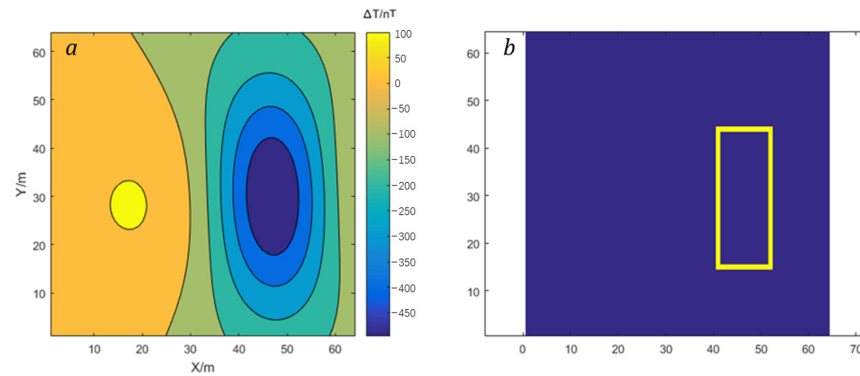


Figure 6. An Example of dataset. (a) Input data (magnetic anomaly). (b) Label data (horizontal projection boundary).

3.2. Training Process

We wrote the code based on Tensorflow (version 2.12.0) and trained the network by GPU (NVIDIA GeForce RTX 3080). The training of a network is the process of updating the weight parameters of the network through the backpropagation mechanism under the constraint of the loss function. This process requires appropriate hyperparameters in order to obtain the optimal network model parameters through continuous iteration. This article mainly selects the parameters shown in Table 2 for training. We chose the mean square error (MSE) as the loss function. The formula of MSE is as follows:

$$MSE = \frac{1}{n} \sum_{i=1}^n (y_i - \hat{y}_i)^2, \quad (2)$$

where n is the total number of labels, y_i is the predicted label, \hat{y}_i is the real label, and i is the order number of the label.

Table 2. Parameter of training networks.

	U-Net EDN	Convolution Block Stacking EDN	ResNet-34 EDN	ResNet-50 EDN
Training set	17,000	17,000	17,000	17,000
Test set	3000	3000	3000	3000
Learning rate	0.0001	0.0001	0.0001	0.0001
Optimizer	Adam	Adam	Adam	Adam
Batch size	32	32	32	32
Epoch	100	100	100	100
Loss function	MSE	MSE	MSE	MSE

The training process of the network is shown in Figure 7.

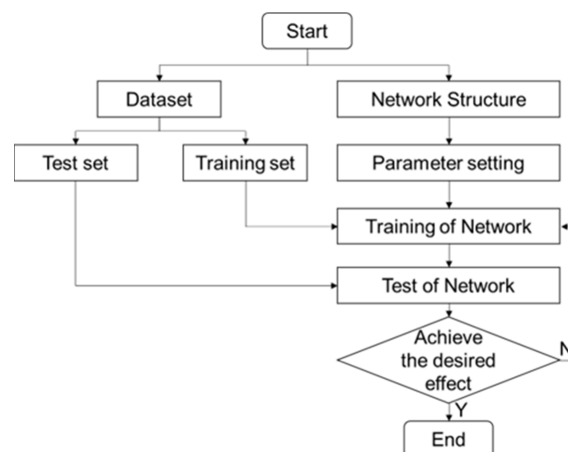


Figure 7. The flowchart of training process.

The training process loss function is shown in Figure 8, and the network model is well trained and basically converges.

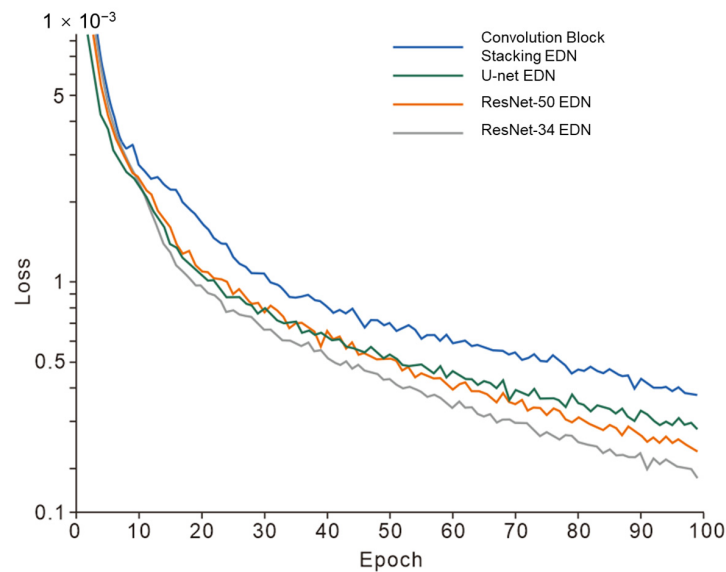


Figure 8. Curve of loss function varying with epoch.

3.3. Evaluation Indicator

The trained network can be used to quickly predict the boundary position of magnetic anomaly field sources. Six sets of experiments are designed in this paper to test and compare the results of four EDNs and traditional edge detection methods. In terms of result evaluation, this article uses accuracy, precision, recall, and F1 score as four evaluation indicators for the predicted results. For the prediction results of the EDNs, there are only two classifications: boundary and background. Therefore, we can consider the problem as a binary classification problem. For a binary classification problem, there are only four combinations between the predicted values and the true values: True Positive (*TP*), False Positive (*FP*), False Negative (*FN*) and True Negative (*TN*). These four types of combinations are shown in Table 3.

Table 3. Binary confusion matrix.

True Value \ Predict Value	Positive	Negative
Positive	<i>TP</i>	<i>FN</i>
Negative	<i>FP</i>	<i>TN</i>

The accuracy formula is as follows:

$$accuracy = \frac{TP+TN}{TP+TN+FP+FN}, \quad (3)$$

The precision formula is as follows:

$$precision = \frac{TP}{TP+FP}, \quad (4)$$

The recall formula is as follows:

$$recall = \frac{TP}{TP+FN}, \quad (5)$$

The F1 score formula is as follows:

$$F1 \text{ Score} = \frac{2 \times precision \times recall}{precision + recall}, \quad (6)$$

4. Data Tests

In this chapter, we are going to test four types of networks (U-net EDN, Convolution block stacking EDN, ResNet-34 EDN, and ResNet-50 EDN) trained by the training set and parameters in Table 2. And the data tests consist of a double combined model, quadruple combined model, overlap model, sphere model and real data.

4.1. Double Combined Model

To consider the comprehensive influence of buried depth and inclined magnetization, two isolated block models are designed, and the parameters of the double combined models are shown in Table 4. The perspective view of the model is shown in Figure 9. Under the background magnetic susceptibility of 0, magnetic inclination and magnetic declination of 60° and 45° , magnetic anomalies were obtained through forward modeling, as shown in Figure 10.

Table 4. The parameters of the double combined models.

Number	1	2
Coordinate of model center point in X, Y, Z direction (m)	(200, 450, 100)	(420, 200, 150)
Model extension length in X, Y and Z direction (m)	(160, 160, 100)	(160, 160, 100)
Magnetic susceptibility (SI)	0.2	0.2

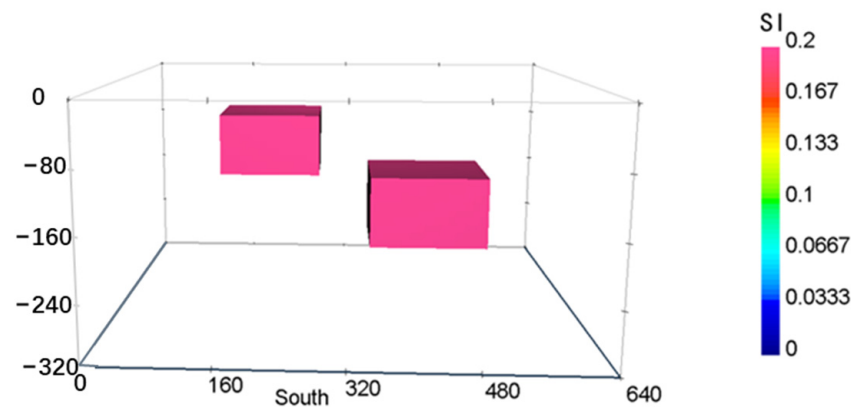


Figure 9. The perspective view of the double combined model.

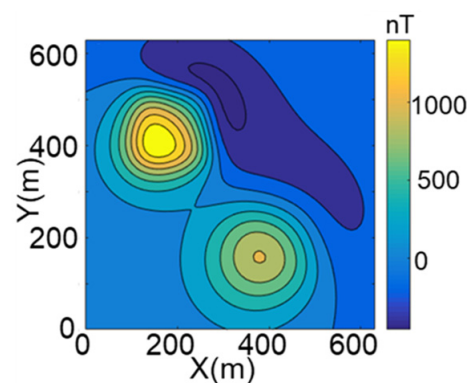


Figure 10. Inclined magnetization anomaly.

The magnetic anomalies are identified using three conventional edge detection methods and four EDNs, and the results are shown in Figure 11. The average evaluation indicators of identified results are shown in Table 5. The properties of the conventional edge detection methods in Figure 11b–d are affected by the comprehensive factors of buried depth and inclination magnetization. In Figure 11e, it can be seen that the convolution

block stacking EDN has poorly identified results for the left and lower boundaries of Model 2 with a deeper burial depth, while the upper and right boundaries are more accurate. In Figure 11f, it can be seen that the U-Net EDN performs well in predicting the overall boundary of Model 2 with a deeper burial depth. It can predict the location and scale of the boundary, but the prediction results are relatively divergent. In Figure 11g,h, it can be seen that the ResNet-50 EDN and ResNet-34 EDN have better prediction results, both of which can accurately identify the boundary positions of anomaly bodies with different burial depths. In comparison, it can be seen from Table 5 that the ResNet-34 EDN still has better prediction results with the highest accuracy and recall.

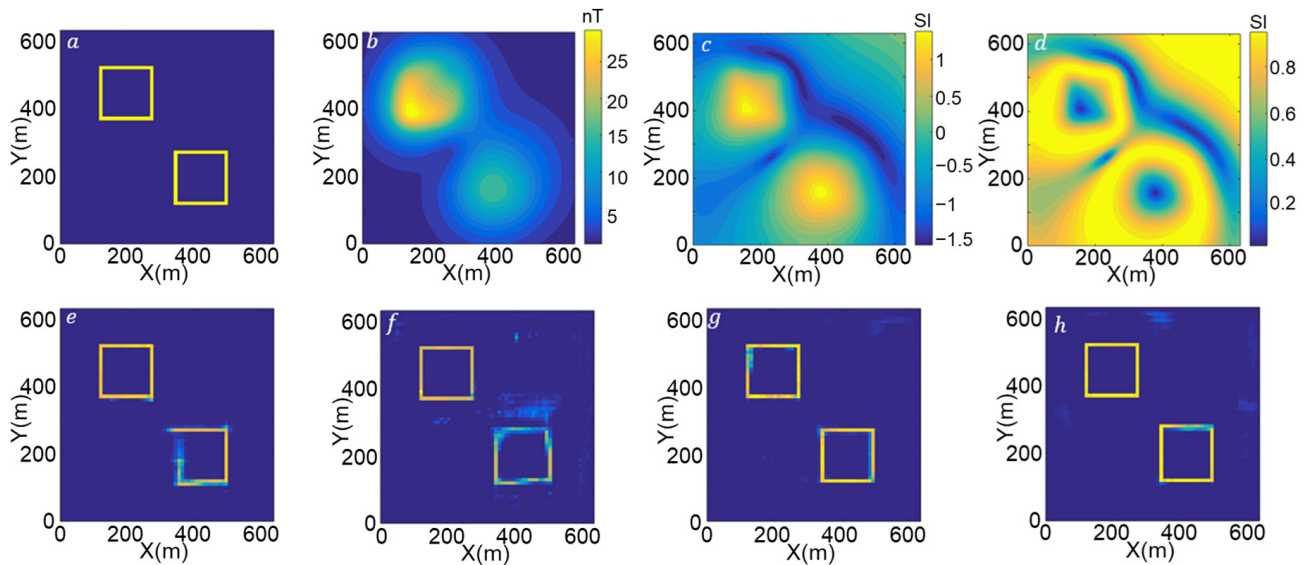


Figure 11. Edge detection results of the double combined model. (a) Ground truth. The yellow boxes present horizontal projection boundaries of the models, while the dark blue pixels present non-boundaries. (b) Analytic signal method. (c) Tilt angle method. (d) Theta map method. (e) Convolution block stacking EDN. (f) U-Net EDN. (g) ResNet-50 EDN. (h) ResNet-34 EDN.

Table 5. Average evaluation indicators of the double combined model in complex situations.

	Accuracy	Precision	Recall	F1 Score
Convolution block stacking EDN	0.9734	0.8939	0.4917	0.6344
U-Net EDN	0.9849	0.7499	0.7250	0.7372
ResNet-50 EDN	0.9873	0.8544	0.7543	0.8012
ResNet-34 EDN	0.9924	0.9376	0.8312	0.8811

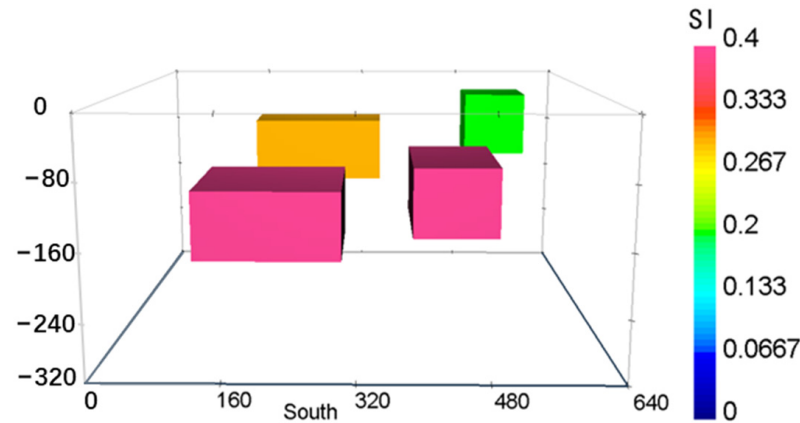
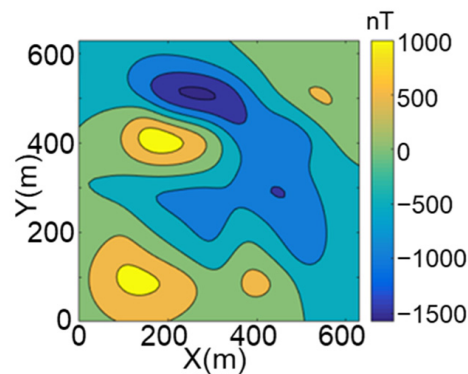
4.2. Quadruple Combined Model

From the results above, it can be concluded that the EDN method for identifying the edge of magnetic anomaly sources is less affected by burial depth and inclined magnetization, and can accurately identify the model boundary position in double combined models. Next, it is necessary to establish a complex model that conforms to the combination of geological bodies to further verify the effectiveness of the EDN method.

A model with four blocks is constructed, considering buried depth, inclined magnetization, magnetic susceptibility and scale. The model parameters are shown in Table 6, and the perspective view of the model is shown in Figure 12. Under the background magnetic susceptibility of 0, magnetic inclination and magnetic declination of 27° and 33° , magnetic anomalies were obtained through forward modeling, as shown in Figure 13.

Table 6. The parameters of the quadruple combined model.

Number	Coordinate of Model Center Point (m)	Model Extension Length (m)	Magnetic Susceptibility (SI)
1	(200, 200, 150)	(200, 200, 100)	0.4
2	(440, 220, 120)	(120, 200, 100)	0.4
3	(250, 470, 100)	(200, 100, 100)	0.3
4	(520, 470, 60)	(100, 100, 100)	0.2

**Figure 12.** The perspective view of the quadruple combined model.**Figure 13.** Complex magnetization anomaly.

The magnetic anomalies are identified using three conventional edge detection methods and four EDNs, and the results are shown in Figure 14. The average evaluation indicators of identified results are shown in Table 7. Due to the mutual influence between the magnetic anomalies of each model and the deviation of magnetic anomaly features caused by inclined magnetization, conventional edge detection methods are affected. Therefore, the three conventional edge detection methods have extremely poor identified performance for the quadruple combined model, and the extracted edge information is greatly deviational and distorted from the actual edge in Figure 14b–d.

Compared with single model and double combined model, the identified effect of EDNs for complex model is reduced, but the approximate location and scale of the model can still be determined in Figure 14e–h. It can be seen that the identified results are gradually improving from Figure 14e to Figure 14h, where ResNet-34 EDN, with the best result, identifies the most accurate and clearest edge of the model. From Table 7, it can also be seen that the evaluation indicators of the ResNet-34 EDN are at the highest level among the four EDNs, with both accuracy and accuracy reaching 0.9. Although the identified result of the ResNet-34 EDN shows a deviation, the small deviation had little effect on determining the boundary position of the model. Therefore, the network can still accurately

identify the boundary positions of magnetic anomaly sources with different burial depths under oblique magnetization.

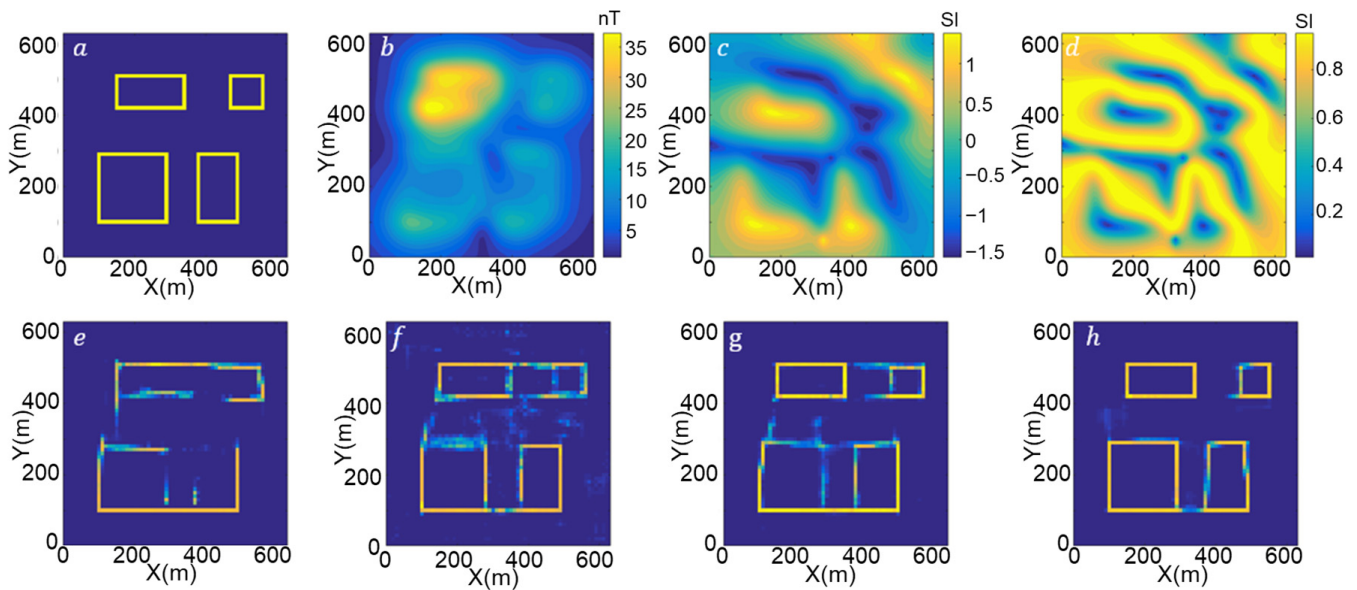


Figure 14. Edge detection results of the quadruple combined model. (a) Ground truth. The yellow boxes present horizontal projection boundaries of the models, while the dark blue pixels present non-boundaries. (b) Analytic signal method. (c) Tilt angle method. (d) Theta map method. (e) Convolution block stacking EDN. (f) U-Net EDN. (g) ResNet-50 EDN. (h) ResNet-34 EDN.

Table 7. Average evaluation indicators of the quadruple combined model.

	Accuracy	Precision	Recall	F1 Score
Convolution block stacking EDN	0.9519	0.5648	0.59210	0.5781
U-Net EDN	0.9585	0.6495	0.5526	0.5971
ResNet-50 EDN	0.9599	0.6495	0.6096	0.6289
ResNet-34 EDN	0.9751	0.9072	0.6769	0.7752

4.3. Overlap Model

Before applying the EDN method to real data, it is necessary to test some special models that are more different from the training set. As the ResNet-34 EDN performed best in the tests above, we will only focus on ResNet-34 EDN and choose overlap models and sphere models to test it. Also, we add noise in the magnetization anomaly to test the robustness.

The overlap model is constructed by two blocks, which overlap vertically. The parameters of the model are shown in Table 8 and the perspective view of the model is shown in Figure 15.

Table 8. The parameters of the overlap model.

Number	Coordinate of Model Center Point (m)	Model Extension Length (m)	Magnetic Susceptibility (SI)
1	(250, 250, 50)	(100, 100, 50)	0.3
2	(320, 320, 125)	(200, 200, 100)	0.3

Under the background magnetic susceptibility of 0, magnetic inclination and magnetic declination is set to 90° and 0° for forward modeling. And we add 5% Gaussian noise to magnetic anomalies. The magnetic anomalies, horizontal projection boundary and Edge detection results are shown in Figure 16.

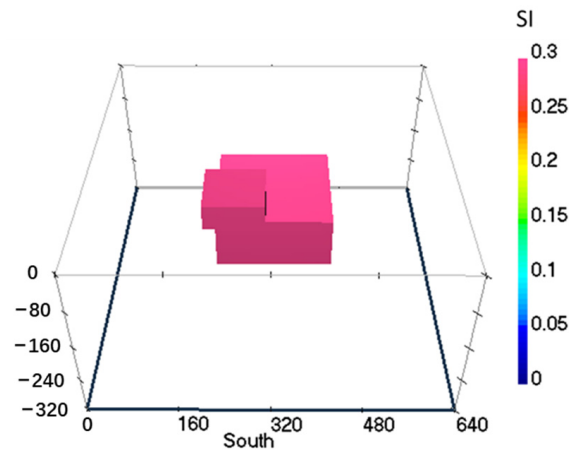


Figure 15. The perspective view of the overlap model.

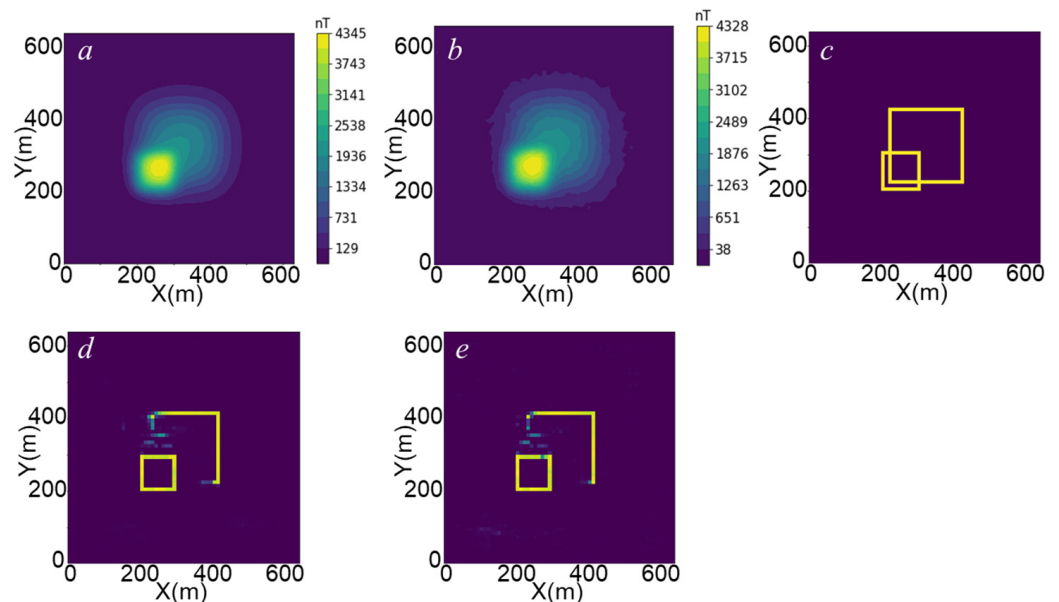


Figure 16. The magnetic anomalies, horizontal projection boundary and edge detection results of the overlap model under magnetic inclination and declination of 90° and 0° . (a) Magnetization anomaly. (b) Magnetization anomaly with 5% Gaussian noise. (c) Ground truth. The yellow boxes present horizontal projection boundaries of the models, while the dark blue pixels present non-boundaries. (d) Edge detection results of (a). (e) Edge detection results of (b).

Next, magnetic inclination and magnetic declination are set to 60° and 45° , while the other parameters are same. The magnetic anomalies, horizontal projection boundary and edge detection results are shown in Figure 17.

From Figure 16d, we can see that the edge of the upper block is detected clearly, while the edge of the lower block is only half displayed. This may be because there was no overlap horizontal projection boundary as the label in the training set and the EDN could not output a result with a crossing line. However, the position prediction of the two blocks is basically accurate. Even if the magnetization anomaly occurs with noise, the detection result is not significantly affected, as shown in Figure 16e.

After the inclination and declination is set to 60° and 45° , the edge of the upper block is detected well as shown in Figure 17d, while the lower one is blurry. In Figure 17e, the edge of the upper block is still clearly visible, while the lower one is very incomplete. Overall, noise has little impact on the results, but the inclination and declination are significantly affected in the overlap situation.

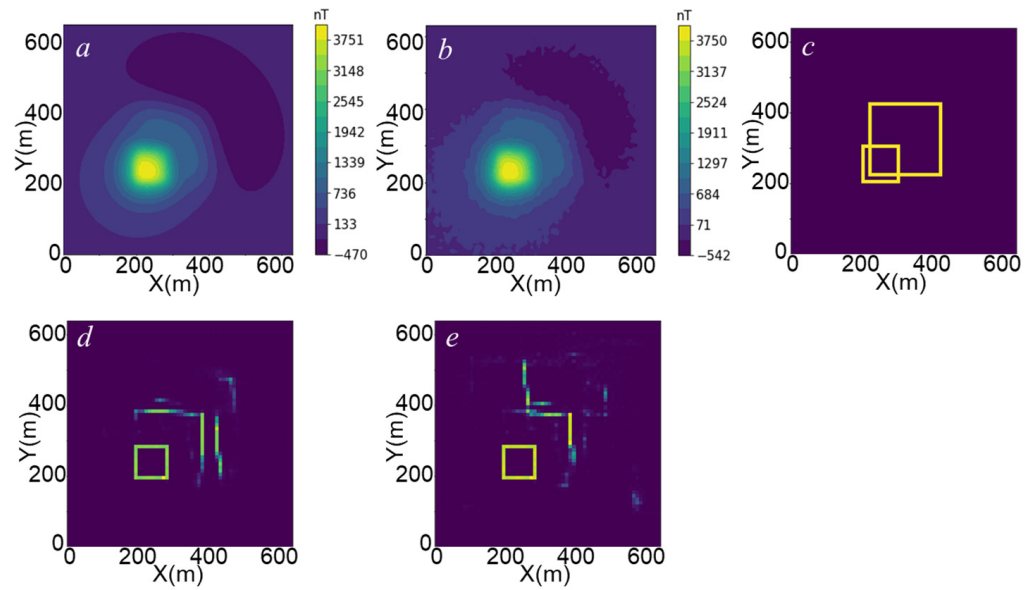


Figure 17. The magnetic anomalies, horizontal projection boundary and edge detection results of the overlap model under magnetic inclination and declination of 60° and 45° . (a) Magnetization anomaly. (b) Magnetization anomaly with 5% Gaussian noise. (c) Ground truth of horizontal projection boundary. (d) Edge detection results of (a). (e) Edge detection results of (b).

4.4. Sphere Model

In the real world, the boundaries of the magnetic source are not always ideally rectangular. We chose a sphere model to test the performance of the EDN with a non-block model.

The parameters of the sphere model are shown in Table 9. The perspective view of the model is shown in Figure 18.

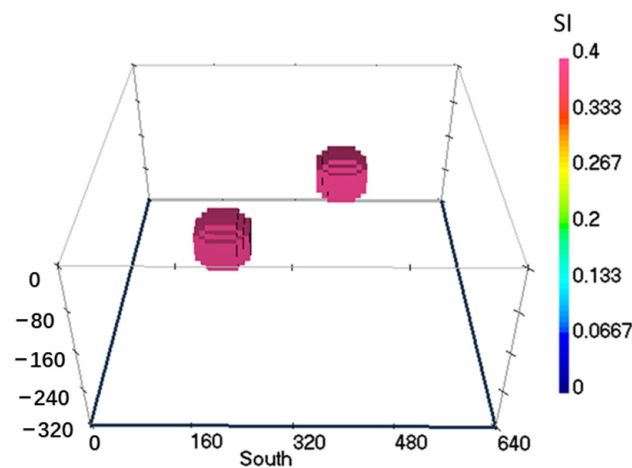


Figure 18. The perspective view of the sphere model.

Table 9. The parameters of the sphere model.

Number	Coordinate of Model Center Point (m)	The Radius of The Sphere (m)	Magnetic Susceptibility (SI)
1	(200, 200, 100)	50	0.4
2	(400, 400, 100)	50	0.4

Magnetic inclination and magnetic declination are set to 90° and 0° for forward modeling and 5% Gaussian noise is added to magnetic anomalies. The magnetic anomalies, horizontal projection boundary and edge detection results are shown in Figure 19.

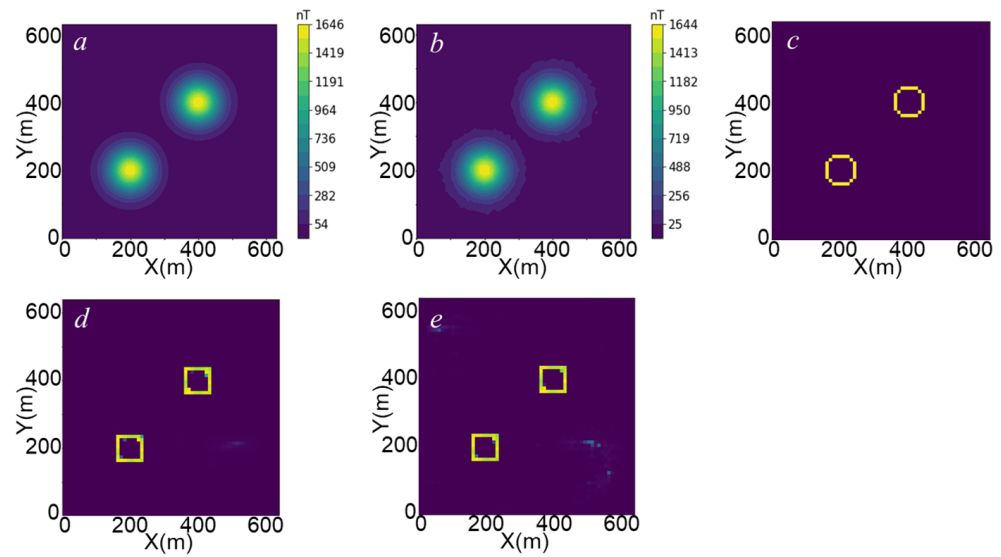


Figure 19. The magnetic anomalies, horizontal projection boundary and edge detection results of sphere model. (a) Magnetization anomaly. (b) Magnetization anomaly with 5% Gaussian noise. (c) Ground truth of horizontal projection boundary. (d) Edge detection results of (a). (e) Edge detection results of (b).

From Figure 19d,e, we can observe that the results show the correct position of two spheres, with a minimal effect of noise, but the boundary is presented as rectangular. When applying the EDN to real data, it is necessary to teach the EDN to draw curved lines. We fine-tuned the ResNet-34 EDN by turning half of the models to spheres in the training set. We trained it for 20 epochs based on the original network parameters while keeping other training parameters in Section 3.2 unchanged. And we tested the ResNet-34 EDN again after fine-tuning. The edge detection results are shown in Figure 20.

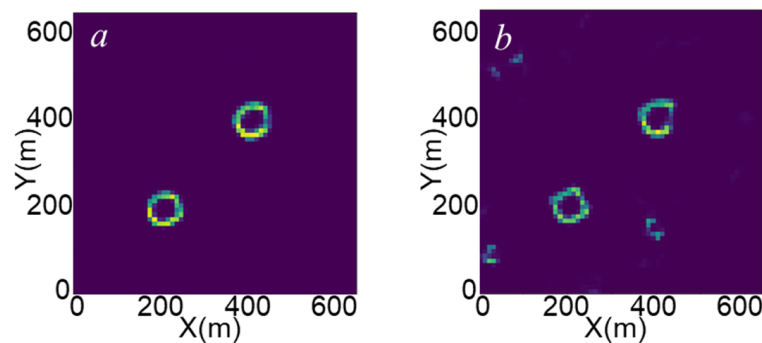


Figure 20. Edge detection results of sphere model after fine-tuning the ResNet-34 EDN. (a) Edge detection results of Figure 19a. (b) Edge detection results of Figure 19b.

From Figure 20a, it can be seen that the boundaries of two sphere models are detected in the correct position and presented by curved lines, which recovered the circle projection boundaries. It can still roughly identify the boundary positions from a magnetic anomaly with noise, as shown in Figure 20b. The robustness of the EDN has been verified. Following fine-tuning, the EDN can output curves and has a certain ability to detect the irregular shape, which could be applied to real data.

4.5. Real Data

The real data are the residual magnetic anomaly data in the South China Sea, which is a Cenozoic marginal sea formed by the expansion of the Mesozoic continental margin background, with widely developed geological structures. The survey area is located in

the north central part of the Pearl River Mouth Basin in the north of the South China Sea, with a longitude range of (112.1–113.3°) and a latitude range of (19.9–21.1°). As shown in Figure 21, this area is the location where igneous rocks are encountered during drilling. Previous research [56] has shown the presence of basic/intermediate-basic and intermediate/intermediate-acid igneous rocks in this area. The horizontal distribution ranges of rocks are shown in the red or green ellipse in Figure 21. This distribution range is similar to that of high-amplitude anomalies. So, we use the data from this survey area to verify the practicality of the EDN method.

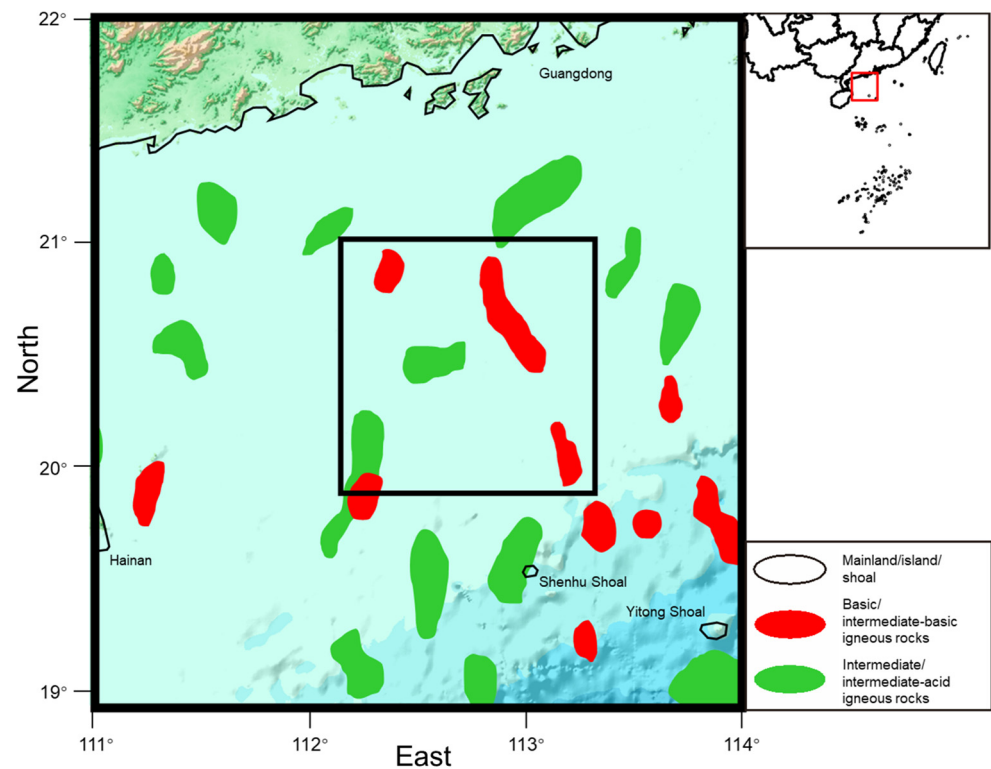


Figure 21. Distribution map of igneous rocks in the northern South China Sea. The smaller black box represents the range of survey area.

The original data are sourced from the compilation materials of the National geological data Museum, with an original scale of 1:200,000. We extracted and processed data in the survey area and gridded the residual magnetic anomaly data into regular data with a size of 64×64 . The contour map is shown in Figure 22. Four methods, including the tilt angle method, theta map method, ResNet-34 EDN and ResNet-34 EDN (after fine-tuning), were used to identify the boundaries of anomalies. The identified results are shown in Figure 23. From the identified results of the conventional edge detection methods, they can identify the boundaries of shallower buried field sources. Both of them can evenly identify the boundaries of source bodies with different burial depths, but the identified resolution is relatively low. The results of ResNet-34 EDN are similar to those of the tilt angle method and theta map method, but the resolution is relatively higher than conventional edge detection methods. The results of ResNet-34 EDN after fine tuning present more closed curves and less discontinuous or dotted lines. The improvement after fine-tuning is not much but the image looks cleaner in appearance. This is in line with our previous conclusion in the tests of different models, that is, the edge detection of a source body from magnetic anomaly based on CNNs is less affected by the burial depth of the source body, and has higher resolution compared to conventional edge detection methods.

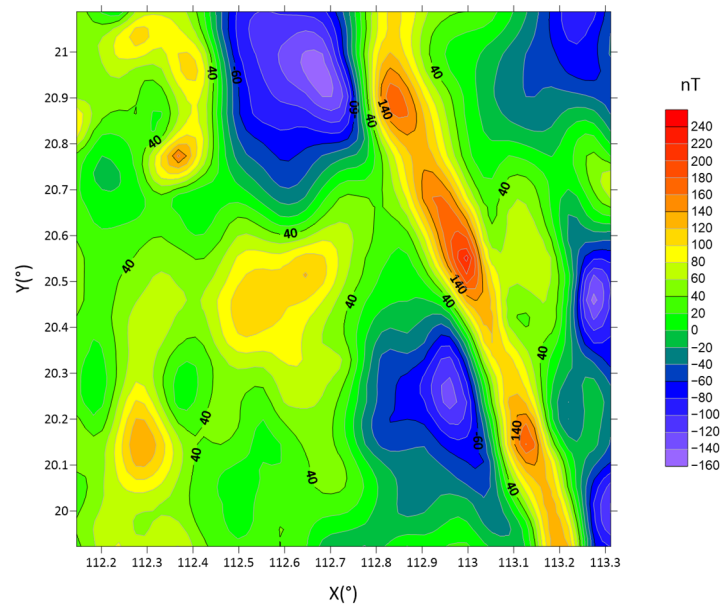


Figure 22. Residual magnetic anomaly of survey area.

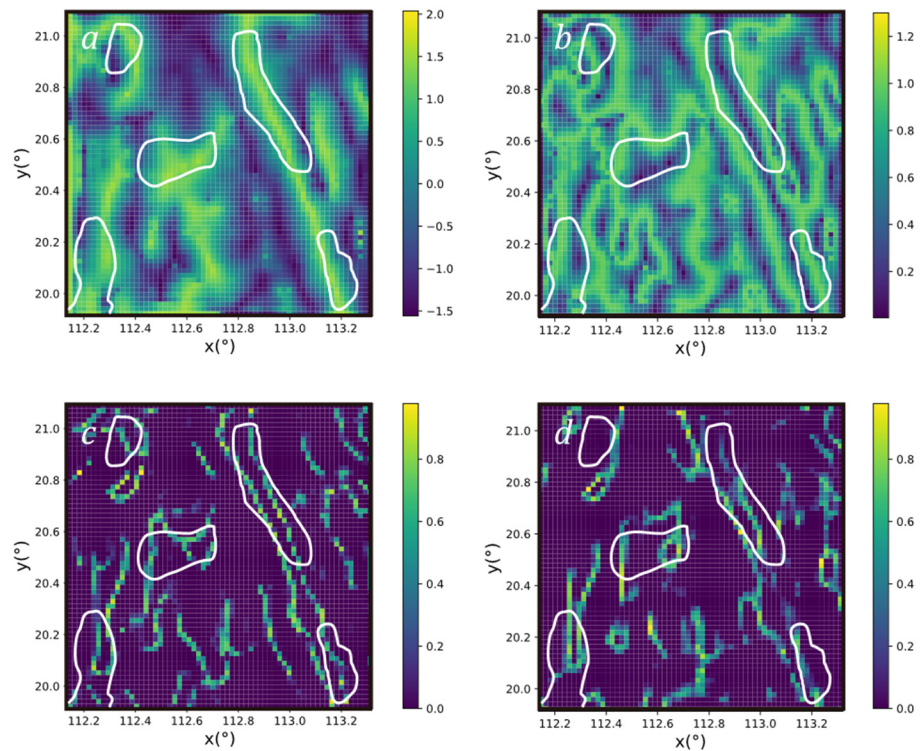


Figure 23. Identified results of residual magnetic anomaly. (a) Tilt angle method. (b) Theta map method. (c) ResNet-34 EDN. Pixel values represent the probability of boundaries. (d) ResNet-34 EDN (after fine tuning). The white line represents the boundary of igneous rocks drawn by predecessors.

5. Conclusions

This paper introduces the image semantic segmentation algorithm and residual block module into the edge detection of magnetic anomaly field bodies. Based on U-Net, four types of EDNs were designed by using convolutional block stacking and residual block module for replacement and modification. The model is parameterized by the number, location, scale, physical properties and other parameters. The magnetic susceptibility model is formed by combining randomly generated parameters, and the forward magnetic

anomaly is generated by forward modeling. The magnetic anomaly is defined as the input data, and the horizontal projection boundary of the field source body is defined as the label data, forming a deep learning dataset. Then, the mapping relationship between the magnetic anomaly and the horizontal projection boundary of the magnetic field source body is studied by the four EDNs.

By establishing six groups of model tests from simple to complex, the effects of buried depth, inclined magnetization and the combination of the two are considered. Firstly, the prediction results of four EDNs are compared with three conventional edge detection methods. The results show that all EDN methods have good performance compared to conventional methods, and are less affected by the burial depth of the field source body. EDNs are able to identify the boundaries of field source bodies with different burial depths more evenly. The influence of inclined magnetization is also relatively small, and the boundary position of the field source body can be identified from magnetic anomalies with shifting. Secondly, the prediction results of four EDNs were evaluated and analyzed using accuracy, precision, recall, and F1 score. The results show that the ResNet-34 EDN based on the conventional residual module performed the best among the four EDNs in model tests. In addition, the robustness of ResNet-34 EDN is verified by a special model with noise. In order to satisfy practical applications of outputting curved lines, the ResNet-34 EDN is fine-tuned using a training set with sphere models. Finally, the effectiveness of this EDN method is further verified by the real data in the Pearl River of the northern South China Sea. The EDN method can present clearer boundaries of igneous rocks directly and does not require manual delineation of the boundaries from the filtered image, which is more convenient for researchers without professional knowledge of geophysics.

Although the ResNet-34 EDN performs well in this paper, there are some obvious limitations of the method. In the test of the overlap model, the method presented the proper location but had difficulty in displaying cross boundaries of an untrained style. Consequently, when applied in real data, the EDN may output unclosed curves, which introduces potential interpretation bias. Furthermore, the results detected by fine-tuning EDN did not show significant improvements. We can infer that the method exhibits a deficiency in the deep optimization of the network. The selection of architecture and hyperparameters is based on human experience and is a locally optimal choice. There is more room for improvement in the future, such as using attention mechanism modules to improve the network architecture. In future work, it is necessary to consider the changes in the shape of the models and add more complex shape models such as ellipsoidal, trapezoidal, crossing, dipping and bishop models.

Author Contributions: Conceptualization, H.C.; methodology, X.Z. and H.C.; software, X.Z. and H.C.; validation, X.Z.; formal analysis, X.Z.; investigation, X.Z.; resources, Z.C.; data curation, X.Z.; writing—original draft preparation, X.Z. and H.C.; writing—review and editing, Z.C., S.W. and Z.O.K.; visualization, X.Z.; supervision, Z.C.; project administration, X.Z.; funding acquisition, Z.C. All authors have read and agreed to the published version of the manuscript.

Funding: This research was supported by the National Natural Science Foundation of China (No. 42274183).

Data Availability Statement: The code can be found at the link https://github.com/forninezexy/edge_detection_of_magnetic_source_by_resnet, accessed on 20 August 2024.

Conflicts of Interest: The authors declare no conflicts of interest.

References

1. Wang, W.; Qiu, Z.; Yang, Y.; Shi, W. Some advances in the edge recognition of the potential field. *Prog. Geophys.* **2010**, *25*, 196–210.
2. Hood, P.; McClure, D. Gradient measurements in ground magnetic prospecting. *Geophysics* **1965**, *30*, 403–410. [[CrossRef](#)]
3. Bhattacharyya, B. Two-dimensional harmonic analysis as a tool for magnetic interpretation. *Geophysics* **1965**, *30*, 829–857. [[CrossRef](#)]
4. Hood, P.J.; Teskey, D.J. Aeromagnetic gradiometer program of the Geological Survey of Canada. *Geophysics* **1989**, *54*, 1012–1022. [[CrossRef](#)]

5. Sertcelik, I.; Kafadar, O. Application of edge detection to potential field data using eigenvalue analysis of structure tensor. *J. Appl. Geophys.* **2012**, *84*, 86–94. [[CrossRef](#)]
6. Evjen, H. The place of the vertical gradient in gravitational interpretations. *Geophysics* **1936**, *1*, 127–136. [[CrossRef](#)]
7. Cordell, L. Gravimetric expression of graben faulting in Santa Fe country and the Espanola basin, New Mexico. In Proceedings of the Guidebook to Santa Fe Country, 30th Field Conference, Santa Fe, NM, USA, 4–6 October 1979; pp. 59–64.
8. Nabighian, M.N. The analytic signal of two-dimensional magnetic bodies with polygonal cross-section: Its properties and use for automated anomaly interpretation. *Geophysics* **1972**, *37*, 507–517. [[CrossRef](#)]
9. Nabighian, M.N. Toward a three-dimensional automatic interpretation of potential field data via generalized Hilbert transforms: Fundamental relations. *Geophysics* **1984**, *49*, 780–786. [[CrossRef](#)]
10. Miller, H.G.; Singh, V. Potential field tilt—A new concept for location of potential field sources. *J. Appl. Geophys.* **1994**, *32*, 213–217. [[CrossRef](#)]
11. Verduzco, B.; Fairhead, J.D.; Green, C.M.; MacKenzie, C. New insights into magnetic derivatives for structural mapping. *Lead. Edge* **2004**, *23*, 116–119. [[CrossRef](#)]
12. Wijns, C.; Perez, C.; Kowalczyk, P. Theta map: Edge detection in magnetic data. *Geophysics* **2005**, *70*, L39–L43. [[CrossRef](#)]
13. Hsu, S.-K.; Sibuet, J.-C.; Shyu, C.-T. High-resolution detection of geologic boundaries from potential-field anomalies: An enhanced analytic signal technique. *Geophysics* **1996**, *61*, 373–386. [[CrossRef](#)]
14. Wang, W.; Pan, Y.; Qiu, Z. A new edge recognition technology based on the normalized vertical derivative of the total horizontal derivative for potential field data. *Appl. Geophys.* **2009**, *6*, 226–233. [[CrossRef](#)]
15. Ma, G.; Huang, D.; Yu, P. Application of improved balancing filters to edge identification of potential field data. *Chin. J. Geophys.* **2012**, *55*, 4288–4295.
16. Yuan, Y.; Huang, D.N.; Yu, Q.L. Using enhanced directional total horizontal derivatives to detect the edges of potential-field full tensor data. *Chin. J. Geophys.* **2015**, *58*, 2556–2565.
17. Yang, G. A new technique for potential-field data processing: Small subdomain filtering. *Oil Geophys. Prospect.* **1995**, *30*, 240–244. (In Chinese)
18. Cooper, G.R.; Cowan, D.R. Edge enhancement of potential-field data using normalized statistics. *Geophysics* **2008**, *73*, H1–H4. [[CrossRef](#)]
19. Wang, Y.; Wang, Z.; Zhang, F.; Zhang, J.; Tai, H.; Guo, C. Edge detection of potential field based on normalized vertical gradient of mean square error ratio. *J. China Univ. Pet.* **2012**, *36*, 86–90.
20. Blakely, R.J.; Simpson, R.W. Approximating edges of source bodies from magnetic or gravity anomalies. *Geophysics* **1986**, *51*, 1494–1498. [[CrossRef](#)]
21. Sykes, M.P.; Das, U.C. Directional filtering for linear feature enhancement in geophysical maps. *Geophysics* **2000**, *65*, 1758–1768. [[CrossRef](#)]
22. Cordell, L.; Grauch, V. Mapping basement magnetization zones from aeromagnetic data in the San Juan Basin, New Mexico. In *The Utility of Regional Gravity and Magnetic Anomaly Maps*; Society of Exploration Geophysicists: Houston, TX, USA, 1985; pp. 181–197.
23. Dwivedi, D.; Chamoli, A. Source Edge Detection of Potential Field Data Using Wavelet Decomposition. *Pure Appl. Geophys.* **2021**, *178*, 919–938. [[CrossRef](#)]
24. Li, Q.; Li, Z.; Shi, Z.; Fan, H. Application of Helbig integrals to magnetic gradient tensor multi-target detection. *Measurement* **2022**, *200*, 111612. [[CrossRef](#)]
25. Prasad, K.N.D.; Pham, L.T.; Singh, A.P.; Eldosouky, A.M.; Abdelrahman, K.; Fnais, M.S.; Gómez-Ortiz, D. A Novel Enhanced Total Gradient (ETG) for Interpretation of Magnetic Data. *Minerals* **2022**, *12*, 1468. [[CrossRef](#)]
26. Cutaneo, C.; Vitale, A.; Fedi, M. Unsupervised boundary analysis of potential field data: A machine learning method. *Geophysics* **2023**, *88*, G57–G65. [[CrossRef](#)]
27. Pham, L.T. A Stable Method for Detecting the Edges of Potential Field Sources. *IEEE Trans. Geosci. Remote Sens.* **2024**, *62*, 1–7. [[CrossRef](#)]
28. Núñez-Demarcó, P.; Bonilla, A.; Sánchez-Bettucci, L.; Prezzi, C. Potential-field filters for gravity and magnetic interpretation: A review. *Surv. Geophys.* **2023**, *44*, 603–664. [[CrossRef](#)]
29. Liu, J.; Li, S.; Jiang, S.; Wang, X.; Zhang, J. Tools for Edge Detection of Gravity Data: Comparison and Application to Tectonic Boundary Mapping in the Molucca Sea. *Surv. Geophys.* **2023**, *44*, 1781–1810. [[CrossRef](#)]
30. Gao, H. Study of Seismic Data Residual Statics and AI Denoising. Ph.D. Thesis, University of Science and Technology of China, Hefei, China, 2018.
31. Wang, Y.; Lu, W.; Liu, J.; Zhang, M.; Miao, Y. Random seismic noise attenuation based on data augmentation and CNN. *Chin. J. Geophys.* **2019**, *62*, 421–433.
32. Chen, B. Research on Denoising of Potential Field Data Based on Deep Convolutional Neural Network. Master's Thesis, China University of Geosciences, Beijing, China, 2020.
33. Aydogan, D. CNNEDGE POT: CNN based edge detection of 2D near surface potential field data. *Comput. Geosci.* **2012**, *46*, 1–8. [[CrossRef](#)]
34. Deng, H.; Hu, X.; Cai, H.; Liu, S.; Peng, R.; Liu, Y.; Han, B. 3D Inversion of Magnetic Gradient Tensor Data Based on Convolutional Neural Networks. *Minerals* **2022**, *12*, 566. [[CrossRef](#)]

35. Araya-Polo, M.; Dahlke, T.; Frogner, C.; Zhang, C.; Poggio, T.; Hohl, D. Automated fault detection without seismic processing. *Lead. Edge* **2017**, *36*, 208–214. [[CrossRef](#)]
36. Wu, X.; Liang, L.; Shi, Y.; Fomel, S. FaultSeg3D: Using synthetic data sets to train an end-to-end convolutional neural network for 3D seismic fault segmentation. *Geophysics* **2019**, *84*, IM35–IM45. [[CrossRef](#)]
37. Puzyrev, V. Deep learning electromagnetic inversion with convolutional neural networks. *Geophys. J. Int.* **2019**, *218*, 817–832. [[CrossRef](#)]
38. Liu, B.; Guo, Q.; Li, S.; Liu, B.; Ren, Y.; Pang, Y.; Guo, X.; Liu, L.; Jiang, P. Deep learning inversion of electrical resistivity data. *IEEE Trans. Geosci. Remote Sens.* **2020**, *58*, 5715–5728. [[CrossRef](#)]
39. Wu, B.; Meng, D.; Wang, L.; Liu, N.; Wang, Y. Seismic impedance inversion using fully convolutional residual network and transfer learning. *IEEE Geosci. Remote Sens. Lett.* **2020**, *17*, 2140–2144. [[CrossRef](#)]
40. Zhang, Z.; Lu, R.; Liao, X.; Xu, Z.; Qiao, Z.; Fan, X.; Yao, Y.; Shi, Z.; Liu, P.; Lu, S. Inversion of magnetic anomaly and magnetic gradient anomaly based on fully convolution network. *Prog. Geophys.* **2021**, *36*, 325–337.
41. Zhang, Z.; Liao, X.; Cao, Y.; Hou, Z.; Fan, X.; Xu, Z.; Lu, R.; Feng, T.; Yao, Y.; Shi, Z. Joint gravity and gravity gradient inversion based on deep learning. *Chin. J. Geophys.* **2021**, *64*, 1435–1452.
42. Zhang, Z.; Yao, Y.; Shi, Z.; Wang, H.; Qiao, Z.; Wang, S.; Qin, L.; Du, S.; Luo, F.; Liu, W. Deep learning for potential field edge detection. *Chin. J. Geophys.* **2022**, *65*, 1785–1801.
43. Zhang, J.; Lin, S.; Ding, L.; Bruzzone, L. Multi-scale context aggregation for semantic segmentation of remote sensing images. *Remote Sens.* **2020**, *12*, 701. [[CrossRef](#)]
44. Guo, M.; Liu, H.; Xu, Y.; Huang, Y. Building extraction based on U-Net with an attention block and multiple losses. *Remote Sens.* **2020**, *12*, 1400. [[CrossRef](#)]
45. Li, Z.; Li, Y.; Wu, X.; Liu, G.; Lu, H.; Tang, M. Hollow village building detection method using high resolution remote sensing image based on CNN. *Trans. Chin. Soc. Agric. Mach* **2017**, *48*, 160–165.
46. Pan, X.; Yang, F.; Pan, G. Extraction of Residential Areas in GF-1 Remote Sensing Images Based on Improved Fully Convolutional Network. *Telecommun. Eng.* **2018**, *58*, 119–125.
47. Wang, Y.; Chen, C.; Ding, M.; Li, J. Real-time dense semantic labeling with dual-Path framework for high-resolution remote sensing image. *Remote Sens.* **2019**, *11*, 3020. [[CrossRef](#)]
48. Lan, M.; Zhang, Y.; Zhang, L.; Du, B. Global context based automatic road segmentation via dilated convolutional neural network. *Inf. Sci.* **2020**, *535*, 156–171. [[CrossRef](#)]
49. Shi, Y.; Wu, X.; Fomel, S. SaltSeg: Automatic 3D salt segmentation using a deep convolutional neural network. *Interpretation* **2019**, *7*, SE113–SE122. [[CrossRef](#)]
50. Ronneberger, O.; Fischer, P.; Brox, T. U-net: Convolutional networks for biomedical image segmentation. In Proceedings of the Medical Image Computing and Computer-Assisted Intervention–MICCAI 2015: 18th International Conference, Munich, Germany, 5–9 October 2015; Part III 18. pp. 234–241.
51. He, K.; Zhang, X.; Ren, S.; Sun, J. Deep residual learning for image recognition. In Proceedings of the IEEE Conference on Computer Vision and Pattern Recognition, Las Vegas, NV, USA, 27–30 June 2016; pp. 770–778.
52. Ioffe, S.; Szegedy, C. Batch normalization: Accelerating deep network training by reducing internal covariate shift. In Proceedings of the International Conference on Machine Learning, Lille, France, 6–11 July 2015; pp. 448–456.
53. Xu, B.; Wang, N.; Chen, T.; Li, M. Empirical evaluation of rectified activations in convolutional network. *arXiv* **2015**, arXiv:1505.00853.
54. Badrinarayanan, V.; Kendall, A.; Cipolla, R. Segnet: A deep convolutional encoder-decoder architecture for image segmentation. *IEEE Trans. Pattern Anal. Mach. Intell.* **2017**, *39*, 2481–2495. [[CrossRef](#)]
55. Guo, Z.H.; Guan, Z.N.; Xiong, S.Q. Cuboid ΔT and its gradient forward theoretical expressions without analytic odd points. *Chin. J. Geophys.* **2004**, *47*, 1277–1285.
56. Wu, X. Study Igneous Rock Distribution of Northern South China Sea by Using Gravity and Magnetic Method. Master's Thesis, Chengdu University of Technology, Chengdu, China, 2016.

Disclaimer/Publisher's Note: The statements, opinions and data contained in all publications are solely those of the individual author(s) and contributor(s) and not of MDPI and/or the editor(s). MDPI and/or the editor(s) disclaim responsibility for any injury to people or property resulting from any ideas, methods, instructions or products referred to in the content.